Atherosclerosis 290 (2019) 94–102

Contents lists available at ScienceDirect

Atherosclerosis

journal homepage: www.elsevier.com/locate/atherosclerosis

Intravascular optical coherence tomography method for automated detection of macrophage infiltration within atherosclerotic coronary plaques

Jose J. Rico-Jimenez[a], Daniel U. Campos-Delgado[b], L. Maximillan Buja[c], Deborah Vela[c], Javier A. Jo[a,d,*]

[a] Department of Biomedical Engineering, Texas A&M University, College Station, TX, USA
[b] Facultad de Ciencias, Universidad Autonoma de San Luis Potosi, SLP, Mexico
[c] Texas Heart Institute, Houston, TX, USA
[d] School of Electrical and Computer Engineering, University of Oklahoma, Norman, OK, USA

HIGHLIGHTS

- An IV-OCT methodology for automated identification of macrophage infiltration.
- The NSD ratio feature of IV-OCT images highlights macrophage infiltration areas.
- CD68 staining was used to correlate macrophages presence with NSD ratio values.

ARTICLE INFO

Keywords:
Atherosclerotic plaque vulnerability
Atherosclerotic plaque imaging
Macrophage infiltration imaging
Intravascular optical coherence tomography
Image analysis

ABSTRACT

Background and aims: Significant macrophages infiltration in advanced atherosclerotic plaques promotes acute coronary events. Hence, the clinical imaging of macrophage content in coronary atherosclerotic plaques could potentially aid in identifying patients most at risk of future acute coronary events. The aim of this study was to introduce and validate a simple intravascular optical coherence tomography (IV-OCT) image processing method for automated, accurate and fast detection of macrophage infiltration within coronary atherosclerotic plaques.
Methods: This method calculates the ratio of the normalized-intensity standard deviation (NSD) values estimated over two axially-adjacent regions of interest in an IV-OCT cross-sectional image (B-scan). When applied to entire IV-OCT B-scans, this method highlights plaque areas with high NSD ratio values (NSDRatio), which was demonstrated to be correlated with the degree of coronary plaque macrophage infiltration.
Results: Using an optimized NSDRatio threshold value, coronary plaque macrophage infiltration could be detected with ~88% sensitivity and specificity in a database of 28 IV-OCT scans from postmortem coronary segments. For comparison, using an optimized NSD threshold value, considered the standard IV-OCT signature for macrophages, coronary plaque macrophage infiltration could be detected with only ~55% sensitivity and specificity.
Conclusions: The proposed NSDRatio method significantly increases the sensitivity and specificity for the detection of coronary plaque macrophage infiltration compared to the standard NSD method. This computationally efficient method can be seamlessly implemented within standard IV-OCT imaging systems for *in-vivo* real-time imaging of macrophage content in coronary plaques, which could potentially aid in identifying patients most at risk of future acute coronary events.

1. Introduction

Intravascular optical coherence tomography (IV-OCT) is a light-scattering based imaging modality that enables high-resolution cross-sectional *in vivo* imaging of coronary arteries [1]. The presence of macrophages (MAC) within coronary atherosclerotic plaques under IV-OCT imaging was first visually associated with signal-rich regions with punctuate bright spots, which lead to a pivotal study that demonstrated a linear correlation between macrophage density in the fibrous cap of fibrotheromas and the IV-OCT signal normalized standard deviation or

* Corresponding author. School of Electrical and Computer Engineering, University of Oklahoma, Stephenson Research and Technology Center, Suite 1108, 101 David L Boren Blvd Norman, OK, 73019, USA.
E-mail address: javierjo@ou.edu (J.A. Jo).

https://doi.org/10.1016/j.atherosclerosis.2019.09.023
Received 27 June 2019; Received in revised form 22 August 2019; Accepted 27 September 2019
Available online 28 September 2019

NSD [2,3], which quantifies the variability of the IV-OCT signal within a predefined region of interest (ROI) as follows:

$$NSD_{ROI} = \frac{\sigma_{ROI}}{S_{max} - S_{min}} \quad (1)$$

and

$$\sigma^2_{ROI} = \frac{1}{N-1} \sum_x \sum_y (S(x,y) - \bar{S})^2 \quad ; S(x,y) \in ROI \quad (2)$$

where S_{max} and S_{min} are the maximum and minimum intensity values of the whole cross-sectional IV-OCT image (B-scan), N is the total number of pixels in the ROI, $S(x, y)$ is the IV-OCT signal as a function of x and y locations within the ROI, and $\bar{S}$ is the mean value of the IV-OCT signal within the ROI. In subsequent studies, the NSD was used to investigate the correlation of plaque fibrous cap macrophage density and clinical syndromes [3] and the presence of thin-cap fibroatheromas [4]. A common limitation of these studies, however, is that the application of NSD was constrained to the fibrous cap of fibroatheromas. Moreover, a later study revealed that bright spots seen in IV-OCT images are not only caused by macrophages but also by other plaque components (including microcalcifications, cholesterol crystals, and/or internal/external elastic membrane), revealing the limited specificity of the NSD for detecting macrophage plaque infiltration [5].

The current consensus standards for IV-OCT image interpretation define the following criteria and guidelines for the visual assessment of macrophage infiltration in IV-OCT images [1]: i) macrophages produce signal-rich regions with punctuate bright spots; ii) macrophage clusters significantly attenuate the OCT signal, shadowing the underlying tissue; iii) macrophages can only be assessed in the context of a fibroatheroma and within the fibrous cap; iv) microcalcifications, cholesterol crystals, and/or internal/external elastic membrane can be confused with macrophages accumulation. Based on these consensus standards, we introduce here a novel and simple IV-OCT image processing method for automated, accurate and fast detection of macrophage infiltration within coronary atherosclerotic plaques.

2. Materials and methods

2.1. Automated IV-OCT based detection of MAC clusters

This novel approach is based on the NSD value calculated from the IV-OCT magnitude signal and has been designed to improve both the sensitivity and the specificity for the detection of macrophage plaque infiltration (MAC-PI) not only in preselected ROIs within the fibrous cap of fibroatheromas, but in the whole IV-OCT plaque image. Following the criteria for the visual identification of macrophages in IV-OCT images described before, this novel methodology aims to identify punctuated signal-rich areas (with high NSD values) followed by signal-attenuated areas or shadows (with low NSD values) in a subsequently deeper axial region. To achieve this, the NSDRatio concept is introduced as follows. Fig. 1A shows two ROIs on an IV-OCT image, one centered at the IV-OCT interrogated pixel (ROI1) and the other at a subsequent deeper axial region (ROI2), with their centers separated by a certain distance or span. The NSDRatio value of the interrogated pixel is simply computed using Eq. (1) and Eq. (2) as:

$$NSD_{Ratio} = \frac{NSD_{ROI1}}{NSD_{ROI2}} \quad (3)$$

Thus, only regions with bright spots (high NSD value in ROI1) followed by a highly attenuated signal in a deeper region (low NSD value in ROI2) will present elevated NSDRatio values, which would be specific to MAC-PI.

Fig. 1B summarizes the steps involved in this novel IV-OCT image processing method for automated MAC-PI detection. First, catheter and lumen-interface artifacts are removed, and the resulting IV-OCT raw-intensity image is normalized (Min-Max) from 0 to 1. Then, the NSD map is calculated by applying a standard-deviation spatial filter of size equal to the ROI's (Fig. 2A). From the NSD map, the NSDRatio map (Fig. 2B) is computed as follows. For a given pixel, its NSDRatio value is calculated as the ratio of NSD values of that pixel (NSD_{ROI1}) and the pixel located at a predefined distance or span deeper in the axial direction (NSD_{ROI2}). A binary mask, computed using the Otsu's segmentation method [6,7] and morphological operations, is applied to remove NSD or NSDRatio values from pixels outside the plaque area. Optimal NSD or NSDRatio threshold values are then applied to the NSD and NSDRatio maps, respectively. Finally, MAC-PI positive pixels ($NSD > Threshold_{NSD}$; $NSDRatio > Threshold_{NSDRatio}$) can be overlaid on the log-compressed IV-OCT images for visualization (Fig. 2C and D).

2.2. Database

IV-OCT images were acquired from 28 cadaveric human coronary artery segments using a swept-source IV-OCT system with a swept range of 115 nm centered at 1320 nm, and a repetition rate of 54 kHz [8,9], resulting in a database of 28 IV-OCT datasets. Each IV-OCT dataset is composed of 9 consecutive B-scans of 1024x1024 pixels (longitudinally spaced by 100 μm), with an axial resolution of 4.8 μm and an angular sampling step of 0.35° [8,9]. The central B-scan (frame 5) of each IV-OCT dataset was rotated to match its corresponding histological section, and the NSD and NSDRatio maps for that central B-scan were computed and matched to the corresponding histological section. Although each artery segment IV-OCT pull-back scan was composed of 9 consecutive B-scans, only the middle B-scan of each pull-back scan was analyzed, since only one histological section (“ground truth”) was obtained from the center of each imaged artery segment. Therefore, a total of 28 B-scans (one per pull-back) and its corresponding histological sections were analyzed in this study.

2.3. Validation

Each CD68 stained histology section was visually reviewed independently for the presence of MAC-PI by three researchers experienced in coronary atherosclerosis histopathology and immunochemistry (L.M.B., J.A.J., D.V.). The lumen on each CD68 stained histology section was marked accordingly, as shown in Fig. 3A, by which red lines along the lumen indicate plaque sectors containing clustered MAC-PI (individual scattered cells were considered MAC-PI negative). Landmarks were visually identified in both the histology section and the corresponding IV-OCT B-scan. These marks were used to manually mark the lumen in the IV-OCT B-scan (red lines in Fig. 3B) based on the histological evaluation (red lines in Fig. 3A) using a custom MATLAB program. The MATLAB program allows the user to manually define the arcs and automatically mark the detected lumen surface based on the dimensions of the arcs. Once the lumen was marked, the program used the histology-guided marked lumen in the IV-OCT B-scan to generate a binary vector of equal size to the number of A-lines in the IV-OCT B-scan, where 1 and 0 denote positive and negative for the presence of clustered MAC-PI, respectively (arcs overlaid on the IV-OCT B-scan, Fig. 3B). This binary vector defines the histology-based classification of each A-line in the IV-OCT B-scan, which was taken as the gold-standard classification. To quantify the performance of each IV-OCT based automated MAC-PI detection method, each A-line was classified as positive for the presence of clustered MAC-PI if at least 10 pixels in the A-line had values above the selected NSD or NSDRatio threshold values (the justification of the 10-pixel threshold is provided in the Supplementary Material, Fig. 1). The IV-OCT based MAC-PI detection for each A-line was also represented as a binary vector, where 1 and 0 denote positive and negative for the presence of clustered MAC-PI, respectively (arcs overlaid on the IV-OCT B-scan, Fig. 3C). By comparing the values of the IV-OCT based MAC-PI detection binary vectors against those of the histology-based evaluation binary vector, the performance of both IV-OCT based automated MAC-PI detection

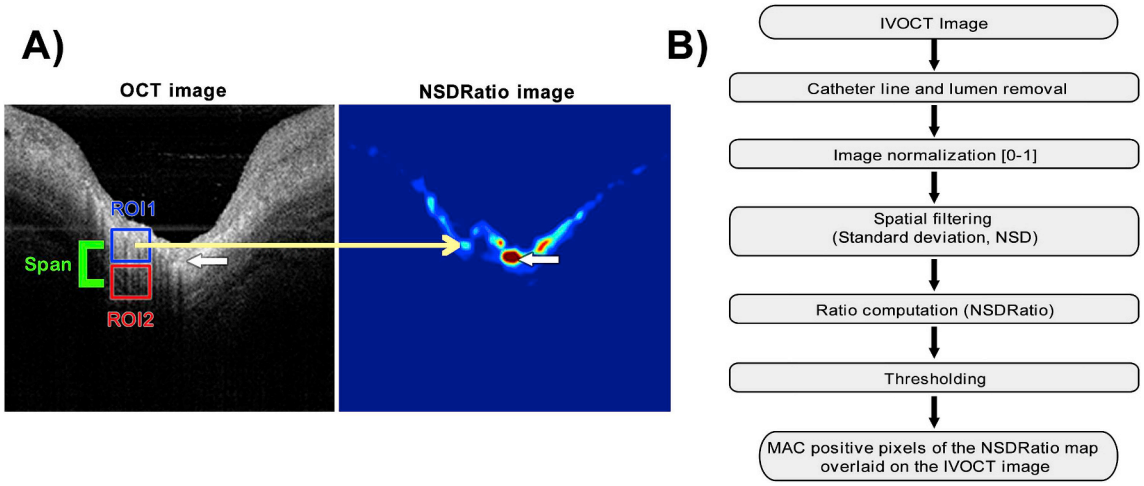

Fig. 1. NSDRatio based method for MAC plaque infiltration detection.
(A) Polar OCT image (left) with overlaid main ROI1 (blue) and preceding ROI2 (red) used to estimate the NSDRatio image (right). Each pixel at the center of ROI1 in the OCT image is transformed into a pixel in the NSDRatio image (yellow arrow). This process is simplified by applying a moving NSD window filter (with the same size as the ROI) to the entire cross-sectional image. Areas with bright spots located above a highly attenuated area produce areas with high NSDRatio values (white arrows). (B) Steps involved in the IV-OCT image processing method for automated detection of MAC-PI.

methods were quantified in terms of sensitivity, specificity, area under the Receiver Operating Characteristic curve (ROC-AUC), and overall accuracy for detecting clustered MAC-PI.

2.4. Threshold and ROI parameter optimization

Optimal values for the NSD or NSDRatio thresholds and the ROI size and span were determined by applying the following analysis. The ROC-AUC for different ROI size and ROI span values were estimated, and the combination of ROI size and ROI span that maximized the ROC-AUC was selected as optimal. For the optimal ROI size-span value combination, the optimal NSD or NSDRatio threshold values were determined as those corresponding to the point in the ROC curve that are closest to the top-left corner, which indicate classification thresholds that would yield the highest accuracy with balanced sensitivity and specificity values.

3. Results

3.1. Threshold and ROI parameter optimization

For the NSDRatio based MAC-PI detection, the ROC-AUC values vary considerably with the ROI size and ROI span values (Fig. 4A), and a maximum ROC-AUC value of 0.932 (white asterisk) was achieved with an ROI size of 51 pixels (244 μm) and an ROI span of 61 pixels (292 μm). For the NSD based MAC-PI detection, the ROC-AUC values of ~0.6 did not change significantly as a function of ROI size; thus, the selection of the ROI size was less critical for the NSD based MAC-PI detection (Fig. 4B). Based on these observations, the ROI size for the NSD and NSDRatio methods were both set to 51 pixels, and the ROI span for the NSDRatio was set to 61 pixels. The ROC curves obtained using these optimal ROI size and span values are shown in Fig. 4C and D for the NSDRatio and NSD based detection methods, respectively. From these ROC curves, the optimal NSDRatio and NSD threshold values were determined as those corresponding to the points (circle marks) in the ROC curves that are closest to the top-left corner (Fig. 4C: $\text{Threshold}_{\text{NSDRatio}}$ = 14.25 folds; Fig. 4D: $\text{Threshold}_{\text{NSD}}$ = 2.4%).

3.2. Performance of the automated IV-OCT-based methods for MAC cluster detection

The classification performance of the NSD and NSDRatio methods was estimated by means of two cross-validation strategies: leave-one out and k-fold. For k-fold cross-validation (k = 7), the database was randomly shuffled and divided in seven parts, 6 parts (24 images) were used for training and 1 part (4 images) for testing, and this process was repeated 10 times. The results from both cross-validations methods are summarized in Table 1, in which mean and standard deviation values of accuracy, sensitivity and specificity were computed from their multiple estimates obtained from each method (28 estimates for leave-one, 10 estimates for k-fold). These performance results clearly indicate that the NSDRatio method outperforms the NSD one (Table 1; Fig. 4). The processing time for both methods (implemented with standard MATLAB R2017a functions of MATLAB R2017a running on a computer with Windows 7 Enterprise 64-bit, CPU Intel i7 with 6 cores at 3.2 GHz, and 48 GB RAM) were also quantified and compared, as shown in Table- 1. Both methods yield virtually the same processing speed of ~5 B-scans/s.

Results of the automated IV-OCT based MAC-PI detection methods using the optimal NSD or NSDRatio threshold values applied to three representative coronary plaques are shown in Fig. 5. The first case corresponds to a fibrotic plaque (Fig. 5A–D). In the CD68 stained histology section (Fig. 5A), superficial (white arrow), deeper (red arrows), and scattered (yellow arrows) MAC-PI clusters can be observed. The superficial MAC-PI cluster was correctly detected by both the NSD and NSDRatio methods (white arrows, Fig. 5C and D). Of the two deeper MAC-PI clusters (red arrows, Fig. 5A), only one was detected by both methods (red arrow in both Fig. 5C and D), while the other one was missed by the two methods (blue arrow in both Fig. 5C and D). The two small scattered MAC-PI clusters (yellow arrows, Fig. 5A) were detected by the NSDRatio method (yellow arrows, Fig. 5D) but missed by the NSD method. The NSD method also produced a false-positive MAC-PI cluster (cyan arrow, Fig. 5C), where no MAC-PI was observed in the CD68 stained histology section (Fig. 5A).

The second case corresponds to a fibroatheroma (Fig. 5E–H)). In the CD68 stained histology section (Fig. 5E), significant MAC-PI can be observed right below the fibrous cap (red arrow). In this region, both the NSD and NSDRatio methods detected MAC-PI, although the detection was more evident for the NSDRatio (red arrows, Fig. 5G and H). The NSD method also produced a very prominent false-positive MAC-PI cluster (purple arrow, Fig. 5G), where no MAC-PI was observed in the CD68 stained histology section (Fig. 5E). The NSDRatio method also showed small and scattered false-positive MAC-PI clusters located outside the plaque area (green arrows, Fig. 5H), which were caused by high signal fluctuations in the intima-media and media-adventitia

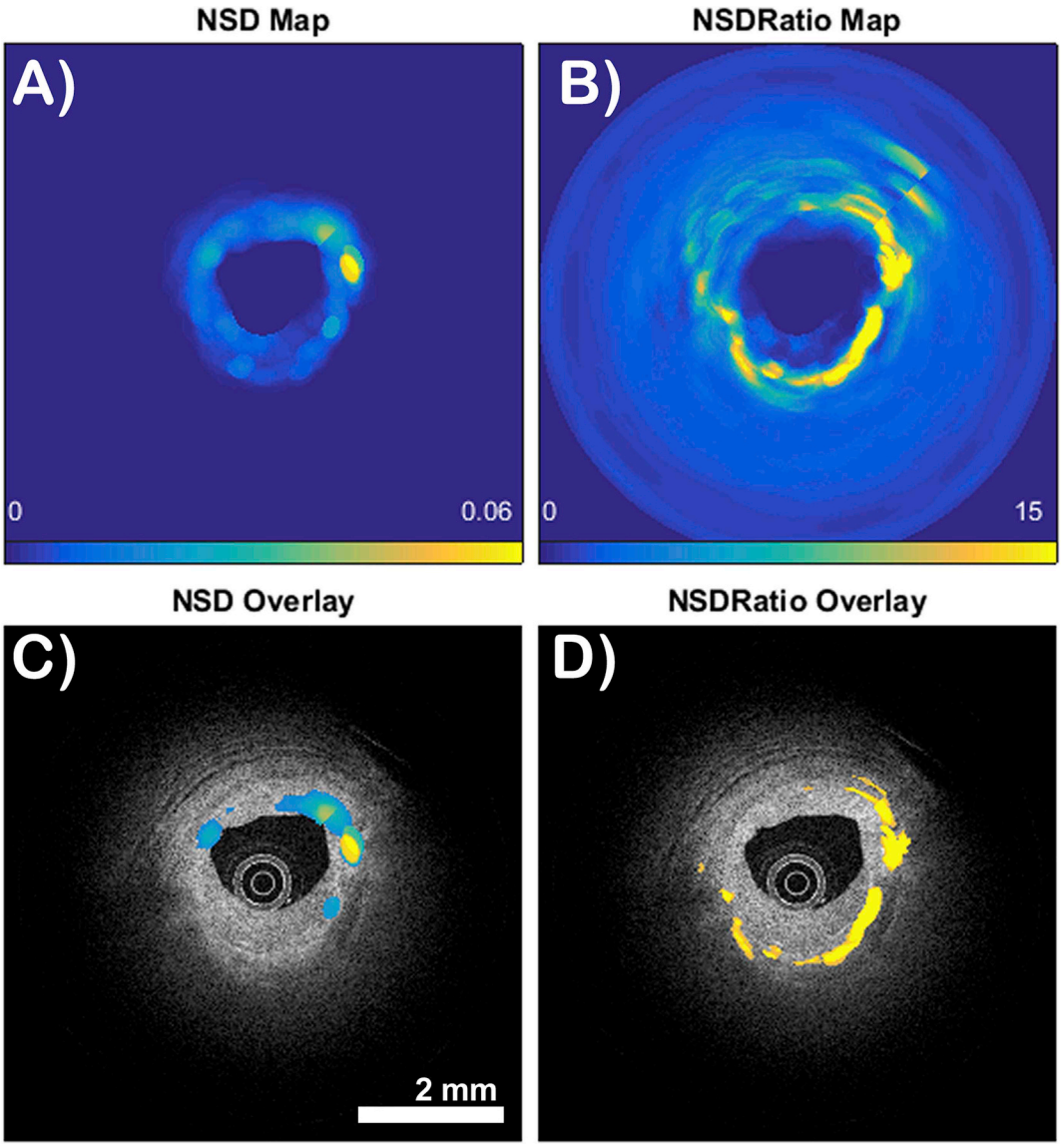

Fig. 2. (A) NSD color-coded map. (B) NSDRatio color-coded map. (C) NSD-threshold based MAC-PI detection overlaid on the log-compressed IV-OCT images for display. (D) NSDRatio-threshold based MAC-PI detection overlaid on the log-compressed IV-OCT images for display.

interfaces.

The third case corresponds to a pathological intimal thickening with significant macrophage infiltration (Fig. 5I to L). In the CD68 stained histology section (Fig. 5I), significant MAC-PI can be observed extending for approximately 65% of the lumen (red arrows). The NSD method detected part of the MAC-PI cluster (red arrow, Fig. 5K), but it missed a large extension of the MAC-PI cluster (blue arrow, Fig. 5K). The NSD method also produced a very prominent false-positive MAC-PI cluster (purple arrows, Fig. 5K), where no MAC-PI presence was observed in the CD68 stained histology section (Fig. 5I). The NSDRatio detected nearly the whole extension of the MAC-PI cluster (red arrows, Fig. 5L), but also presented small false-positive MAC-PI clusters located outside the plaque area caused by high signal fluctuations in the intima-media and media-adventitia interfaces (green arrow, Fig. 5L).

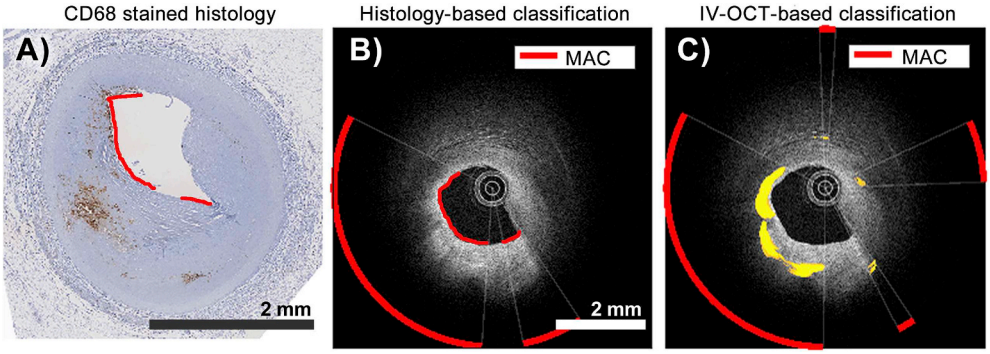

Fig. 3. Histology-based and IV-OCT-based classification.
(A) CD68 stained histological image of a sample human coronary segment with the lumen marked to indicate the presence of MAC-PI based on histopathological evaluation. (B) Graphical representation of A-lines identified as positive for MAC-PI based on histopathological evaluation (red arcs on the IV-OCT image). (C) IV-OCT based classification overlaid on the IV-OCT image; arcs indicate the A-lines automatically classified as positive for MAC-PI.

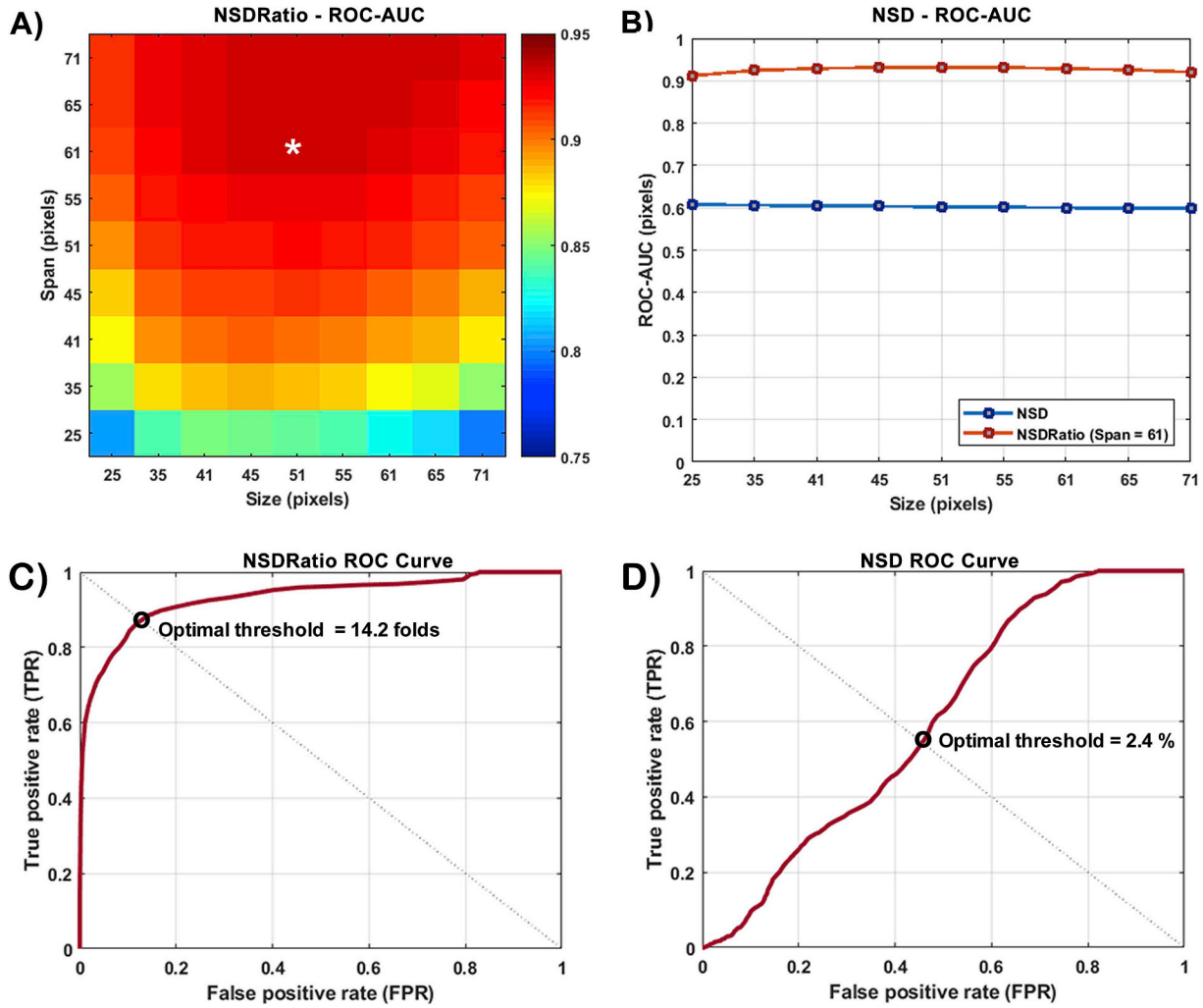

Fig. 4. Optimal threshold and ROI parameter value determination.
(A) ROC-AUC value as a function of ROI size and span for the NSDRatio-based classification. The asterisk mark indicates optimal ROI size (51 pixels, 244 μm) and span (61 pixels, 292 μm) values that led to the highest ROC-AUC value. (B) ROC-AUC value as a function of ROI size for the NSD-based classification. (C) ROC curve for the NSDRatio method applied using the optimal ROI size and span values (circle mark indicates the optimal NSDRatio threshold of 14.2 folds). (D) ROC curve for the NSD method applied using the optimal ROI size value (circle mark indicates the optimal NSD threshold of 2.4%).

3.3. Linear correlation analysis

Linear correlation analysis was performed to quantify a potential linear relation between the degree of MAC-PI quantified between the histology-based evaluation and the automated IV-OCT based MAC-PI detection methods. For all three MAC-PI evaluation/detection methods (histology, NSD, NSDRatio), the degree of MAC-PI was simply quantified as the percentage of A-lines in a given IV-OCT B-scan classified as positive for the presence of MAC-PI, resulting on 28 values of the degree of MAC-PI per evaluation/detection method (one per each imaged coronary segment). Pearson linear correlation analysis was applied to these quantities estimated from the histology-based evaluation and either the NSD or NSDRatio based detection methods. The degree of MAC-PI quantified using NSD was not statistically significantly linearly correlated with the histology-based quantification, as shown in Fig. 6A ($R = 0.19$, $p > 0.3$). On the other hand, the degree of MAC-PI quantified using NSDRatio was statistically significantly linearly correlated with the histology-based quantification, as shown in Fig. 6B ($R = 0.86$, $p < 4.7*10^{-9}$).

Table 1
ROC-based classification performance: leave-one-out validation (LOO-CV); K-fold validation (KF-CV).

		Accuracy (%)	Sensitivity (%)	Specificity (%)	Processing time* (s)
LOO-CV	NSD	54.7 ± 1.2	52.82 ± 1.2	55.28 ± 1.3	~0.180 ± 0.0121
	NSDRatio	88.21 ± 0.4	84.97 ± 0.8	89.23 ± 0.6	~0.182 ± 0.0123
KF-CV (k = 7)	NSD	55.06 ± 1.9	52.35 ± 1.9	55.93 ± 2.0	
	NSDRatio	87.45 ± 0.6	85.57 ± 0.7	88.03 ± 0.6	

*Time to process one IV-OCT B-scan.

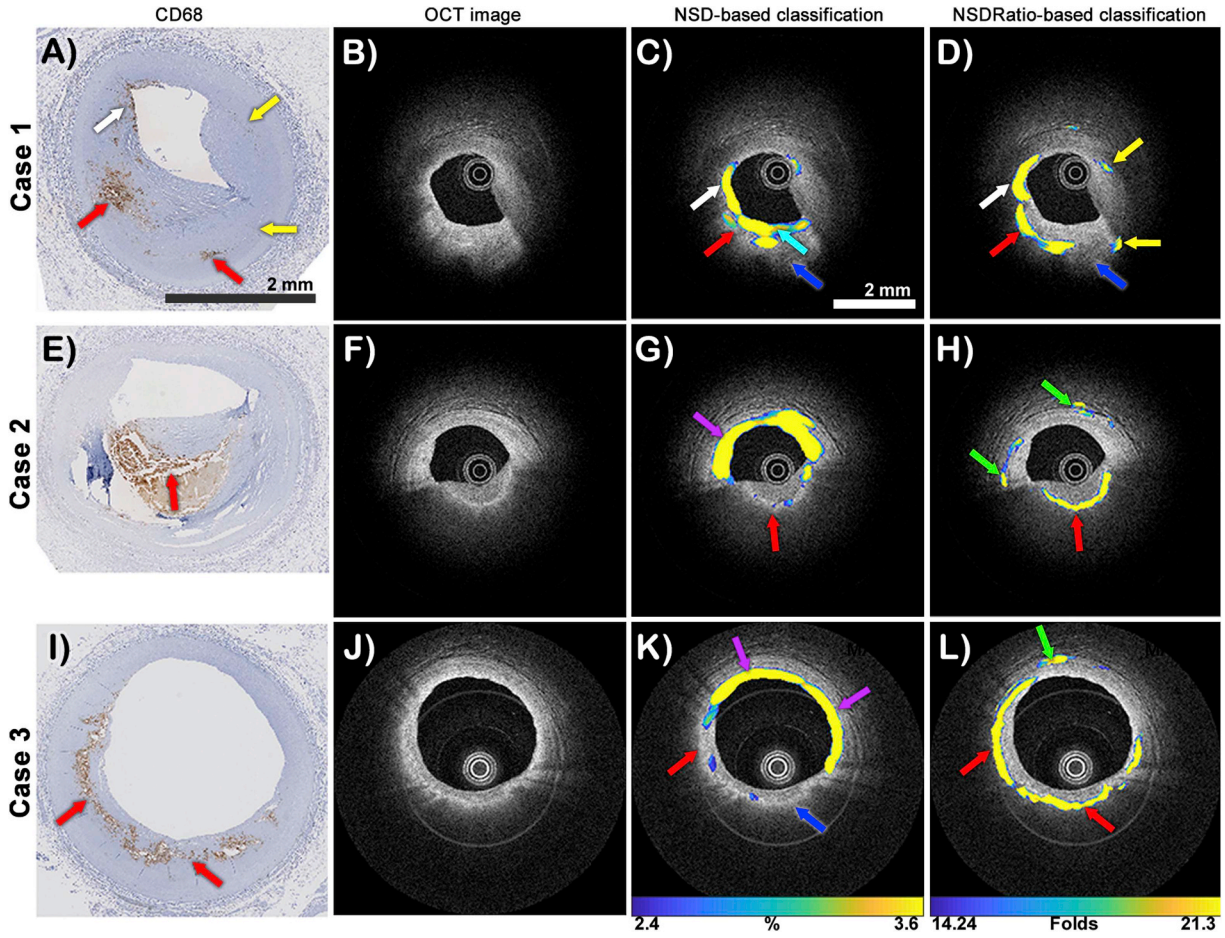

Fig. 5. Classification results for three sample plaques with different degree of MAC-PI.
First column: CD68 histological images. Second column: Original OCT image. Third column: NSD classification maps. Fourth column: NSDRatio classification maps. (A-D) Results of a fibrotic plaque presenting superficial, deeper, and scattered MAC-PI. (E-H) Results of a fibroatheroma presenting significant MAC-PI between the fibrous cap and the top of the necrotic core. (I-L) Results of a pathological intimal thickening presenting a well-defined MAC-PI area covering ~65% of the artery lumen. Arrows: superficial MAC-PI (white), deeper MAC-PI (red), scattered MAC-PI (yellow), false negative (blue), false positive (green and purple).

4. Discussion

We report a simple and computationally efficient IV-OCT image processing method for automated, accurate and fast detection of macrophage infiltration within coronary atherosclerotic plaques. This method calculates the NSDRatio as the ratio of the NSD values estimated over two axially-adjacent regions of interest in an IV-OCT B-scan. When applied to entire IV-OCT B-scans, this method highlights plaque areas with high NSDRatio values, which was demonstrated to be linearly correlated with the degree of coronary MAC-PI. Moreover, using an optimized NSDRatio threshold value, coronary MAC-PI could be detected with almost 90% sensitivity and specificity.

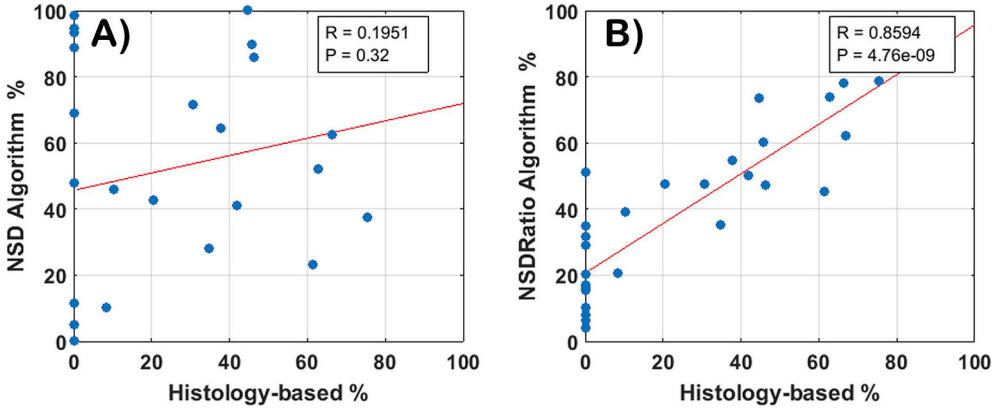

Fig. 6. Pearson's linear correlation analysis between the degree of MAC-PI quantified from the histology-based evaluation and the IV-OCT-based automated MAC-PI detection methods.
(A) NSD based quantification. (B) NSDRatio based quantification.

The pivotal study by Tearney and colleagues established for the first time the correlation between signal-rich IV-OCT image regions with punctuate bright spots with the presence of macrophage in fibroatheromas' fibrous caps, and introduced the NSD as an imaging biomarker for MAC-PI [2,3]. The application of the NSD, however, has been limited to preselected IV-OCT regions of interest mostly within the fibrous cap of fibroatheromas [3,4,10,11]. Moreover, other plaque tissue components can also produce high NSD values leading to poor MAC-PI detection performance [5]. Our results also indicated that NSD based MAC-PI detection, when applied to the whole plaque extension and not only to fibrous caps, shows modest levels (< 60%) of sensitivity and specificity (Fig. 4D and Table 1).

The current consensus standards for the visual assessment of macrophages in IV-OCT images [1] provide the foundation of the proposed NSDRatio based MAC-PI detection method, which overcomes the main limitations of the NSD method. First, since the NSDRatio can be computed for each pixel of the IV-OCT B-scan, NSDRatio maps co-registered with the IV-OCT B-scans can be seemingly generated to provide visualization of areas with significant MAC-PI in the full extension of the plaque tissue (Figs. 2 and 5). Second, since only regions with bright spots followed by a highly attenuated signal in a deeper region will present elevated NSDRatio values, this new metric is more sensitive and specific for detecting MAC-PI compared to the NSD (Fig. 4D and Table 1). Lastly, since the $Threhold_{NSDRatio}$ value is selected from data-generated ROC curves, the $Threhold_{NSDRatio}$ can be biased based on clinical insight to favor either sensitivity or specificity. In this study, the applied $Threhold_{NSDRatio}$ was selected in order achieve balanced levels of sensitivity and specificity for detecting MAC-PI.

In addition to its capability to accurately detect coronary MAC-PI, another advantage of the NSDRatio is its simplicity. Since this method only involves generating NSDRatio maps and applying a predefined $Threhold_{NSDRatio}$, detection and visualization of plaque regions exhibiting significant MAC-PI can be performed in real time (Table 1, Media-S1 of the Supplemental Material). This study also demonstrated a strong linear correlation between the NSDRatio and the degree of coronary MAC-PI (Fig. 6). Based on these results, a calibration curve that would enable quantifying the degree of MAC-PI based on the NSDRatio values is currently being validated; thus, this novel NSDRatio method could potentially enable real-time quantification and visualization of the degree of coronary MAC-PI.

In advanced atherosclerotic lesions, macrophages have an impaired ability to efferocytose apoptotic cells [12,13], and macrophage apoptosis and necrosis is increased [14,15], both factors contributing to plaque necrosis and increased inflammation. Macrophages also secrete matrix metalloproteinases, which can contribute to fibrous cap thinning and plaque rupture [16]. Thus, macrophages play key roles in the development and destabilization of advanced coronary atherosclerotic plaques, and thereby promote acute cardiovascular events [17]. Moreover, the improved understanding of macrophages biology in advance atherosclerotic lesions is enabling exploring other therapeutic alternatives targeting proatherogenic mechanisms in macrophages, which could complement current lipid-lowering therapies and further reduce the risk of cardiovascular events [18–20].

Hence, the clinical imaging and quantification of MAC-PI could potentially assist in identifying high-risk atherosclerotic plaques prone to future coronary events in patients with cardiovascular disease [17,21,22]. Moreover, the pre-clinical and clinical imaging of MAC-PI will also be necessary for evaluating the effectiveness of new therapeutic strategies targeting proatherogenic mechanisms in macrophages before committing to expensive and long-term end point trials [21]. Therefore, this novel IV-OCT image-analysis based method for automated, accurate and fast detection of macrophage infiltration within coronary atherosclerotic plaques will enhance the capabilities of IV-OCT as an intravascular imaging tool for assisting with both identifying patients most at risk of future coronary events and assessing efficacy of potential therapeutic strategies.

Finally, one major challenge in the management of patients coronary atherosclerosis is the accurate prediction of future acute coronary events. Ongoing longitudinal studies, such as the CLIMA study [23], are making an effort to discover and validate imaging-driven plaque vulnerability criteria that could provide personalized scores that could quantify the risk for acute coronary events at the individual patient level. The ongoing CLIMA study is evaluating the effectiveness of a risk scoring system based on several IV-OCT imaging biomarkers concurrently quantified in the same plaque. One of the key IV-OCT biomarkers being considered in the CLIMA study is precisely the presence of macrophage plaque infiltration, which is visually assessed in that study. The application of our method for automated detection of macrophage plaque infiltration would facilitate the CLIMA and other such studies, and could ultimately enable developing much needed quantitative methods for predicting acute coronary events.

4.1. Study limitations

One limitation of this study is the relatively small size of the database of IV-OCT images used for quantifying the accuracy of our proposed method. Although this database provided a plurality of coronary atherosclerotic plaque histopathological phenotypes, a study on a larger database of IV-OCT coronary artery images acquired with commercial IV-OCT imaging systems should be followed to confirm the performance of the NSDRatio method for automated, accurate and fast detection of coronary MAC-PI. Ultimately, *in vivo* clinical studies will need to be also performed to demonstrate the value of the NSDRatio as a imaging biomarker for identifying patients most at risk of future clinical events and assessing efficacy of potential therapeutic strategies.

Another limitation of this study is the fact that the histological evaluation was only performed along the circumferential direction. A histological evaluation identifying the presence of macrophages along both the circumferential and axial (depth) directions would have been more comprehensive; however, correlating positive regions between histological sections and B-scans in both dimensions would have added subjectivity and complexity to the method performance estimation. Therefore, as a first attempt, we decided to limit the correlation to the circumferential direction only, which still allowed us to quantify the method's capability to detect A-lines positive for the presence of macrophages.

Although our method is capable of detecting the presence of macrophages within plaques, it cannot differentiate the context in which macrophage infiltrations are present (e.g. fibrous plaque vs. fibroatheromas). Integrating this method with others aiming to specifically detect fibrous caps, however, would potentially allow the differentiation between macrophages in fibrous plaques versus in fibroatheromas.

One limitation of the current implementation of the NSDRatio is its sensitivity to abrupt IV-OCT signal variations not associated to macrophages, in particular those present in the media-adventitia interface and the connective tissue. These specific signal variations also produce high NSDRatio values that can lead to false positives (green arrows in Fig. 5F and I). Although these false positives reduce the specificity of the NSDRatio, they are usually located in regions outside the plaque area. Automated segmentation of the plaque area within each IV-OCT B-scan [24,25] would enable ignoring these false positive areas, thus increasing the accuracy of the NSDRatio method.

The position of the catheter, particularly when it is in close proximity to the plaque surface, could introduce artifacts in the OCT signal that would potentially affect the performance of our method. The potential effect of the catheter position on our method's performance could not be quantified with the available IV-OCT database, but it should be assessed in future studies.

Finally, during *in vivo* IV-OCT imaging, several imaging artifacts could introduce A-line intensity fluctuations that could be difficult to compensate. Nevertheless, since the NSDRatio depends primarily on the

axial signal attenuation regardless of the energy per A-line, it is expected that the NSDRatio calculation would be less sensitive to most common imaging artifacts, including those related to suboptimal flushing, heart beat motion, and uncontrolled variations of the IV-OCT catheter-to-lumen distance. Future *in vivo* studies, however, will also be needed to quantify the robustness of the NSDRatio to imaging artifacts.

4.2. Conclusions

The proposed NSDRatio method significantly increases the sensitivity and specificity for the detection of MAC-PI compared to the standard NSD method. This computationally efficient method can be seamlessly implemented within commercial IV-OCT imaging systems to enable *in vivo* real-time imaging of macrophage content in coronary plaques, which could potentially aid in i) identifying patients most at risk of future acute coronary events, and ii) assessing efficacy of novel therapeutic strategies.

Financial support

This project was supported by the National Institutes of Health (NHLBI: 1R01HL111361; NCI: 1R01CA218739); TAMU-CONACYT Collaborative Research Grant Program (2015–023).

Author contributions

J.J. Rico-Jimenez: Co-designed the data analysis methodology; analyzed the data, wrote the manuscript. D.U. Campos-Delgado: Co-designed the data analysis methodology; co-edited the manuscript. M. Buja, D. Vera: Performed independent immunohistological evaluation. D. Vera: Performed independent immunohistological evaluation. J.A. Jo: Designed and coordinated the research study; performed independent the immunohistological evaluation; co-edited the manuscript.

Declaration of competing interest

The authors declared they do not have anything to disclose regarding conflict of interest with respect to this manuscript.

Acknowledgments

We acknowledge Drs. Brett E. Bouma and Martin Villiger from the Center for Biomedical OCT Research and translation, funded through NIH-NIBIB P41EB014903, for providing the IV-OCT and histology database used in this study.

Appendix A. Supplementary data

Supplementary data to this article can be found online at https://doi.org/10.1016/j.atherosclerosis.2019.09.023.

References

[1] G.J. Tearney, E. Regar, T. Akasaka, T. Adriaenssens, P. Barlis, H.G. Bezerra, B. Bouma, N. Bruining, J. Cho, S. Chowdhary, M.A. Costa, R. de Silva, J. Dijkstra, C. Di Mario, D. Dudeck, E. Falk, M.D. Feldman, P. Fitzgerald, H. Garcia, N. Gonzalo, J.F. Granada, G. Guagliumi, N.R. Holm, Y. Honda, F. Ikeno, M. Kawasaki, J. Kochman, L. Koltowski, T. Kubo, T. Kume, H. Kyono, C.C.S. Lam, G. Lamouche, D.P. Lee, M.B. Leon, A. Maehara, O. Manfrini, G.S. Mintz, K. Mizuno, M. Morel, S. Nadkarni, H. Okura, H. Otake, A. Pietrasik, F. Prati, L. Räber, M.D. Radu, J. Rieber, M. Riga, A. Rollins, M. Rosenberg, V. Sirbu, P.W.J.C. Serruys, K. Shimada, T. Shinke, J. Shite, E. Siegel, S. Sonada, M. Suter, S. Takarada, A. Tanaka, M. Terashima, T. Troels, S. Uemura, G.J. Ughi, H.M.M. van Beusekom, A.F.W. van der Steen, G.-A. van Es, G. van Soest, R. Virmani, S. Waxman, N.J. Weissman, G. Weisz, Consensus standards for acquisition, measurement, and reporting of intravascular optical coherence tomography studies: a report from the international working group for intravascular optical coherence tomography standardization and validation, J. Am. Coll. Cardiol. 59 (2012) 1058–1072, https://doi.org/10.1016/J.JACC.2011.09.079.

[2] G.J. Tearney, H. Yabushita, S.L. Houser, H.T. Aretz, I.-K. Jang, K.H. Schlendorf, C.R. Kauffman, M. Shishkov, E.F. Halpern, B.E. Bouma, Quantification of macrophage content in atherosclerotic plaques by optical coherence tomography, Circulation 107 (2003) 113–119.

[3] B.D. MacNeill, I.-K. Jang, B.E. Bouma, N. Iftimia, M. Takano, H. Yabushita, M. Shishkov, C.R. Kauffman, S.L. Houser, H.T. Aretz, D. DeJoseph, E.F. Halpern, G.J. Tearney, Focal and multi-focal plaque macrophage distributions in patients with acute and stable presentations of coronary artery disease, J. Am. Coll. Cardiol. 44 (2004) 972–979, https://doi.org/10.1016/J.JACC.2004.05.066.

[4] O.C. Raffel, G.J. Tearney, D.D. Gauthier, E.F. Halpern, B.E. Bouma, I.-K. Jang, Relationship between a systemic inflammatory marker, plaque inflammation, and plaque characteristics determined by intravascular optical coherence tomography, Arterioscler. Thromb. Vasc. Biol. 27 (2007) 1820–1827, https://doi.org/10.1161/ATVBAHA.107.145987.

[5] J.E. Phipps, D. Vela, T. Hoyt, D.L. Halaney, J.J. Mancuso, L.M. Buja, R. Asmis, T.E. Milner, M.D. Feldman, Macrophages and intravascular OCT bright spots: a quantitative study, JACC Cardiovasc. Imaging 8 (2015) 63–72 https://doi.org/10.1016/j.jcmg.2014.07.027.

[6] N. Otsu, A threshold selection method from gray-level histograms, IEEE Trans. Syst. Man. Cybern. 9 (1979) 62–66, https://doi.org/10.1109/TSMC.1979.4310076.

[7] G.J. Ughi, T. Adriaenssens, P. Sinnaeve, W. Desmet, J. D'hooge, Automated tissue characterization of in vivo atherosclerotic plaques by intravascular optical coherence tomography images, Biomed. Opt. Express 4 (2013) 1014–1030, https://doi.org/10.1364/BOE.4.001014.

[8] S.H. Yun, G.J. Tearney, B.J. Vakoc, M. Shishkov, W.Y. Oh, A.E. Desjardins, M.J. Suter, R.C. Chan, J.A. Evans, I.-K. Jang, N.S. Nishioka, J.F. de Boer, B.E. Bouma, Comprehensive volumetric optical microscopy in vivo, Nat. Med. 12 (2006) 1429–1433, https://doi.org/10.1038/nm1450.

[9] M. Villiger, E.Z. Zhang, S.K. Nadkarni, W.-Y. Oh, B.J. Vakoc, B.E. Bouma, Spectral binning for mitigation of polarization mode dispersion artifacts in catheter-based optical frequency domain imaging, Opt. Express 21 (2013), https://doi.org/10.1364/OE.21.016353 16353.

[10] A. Boi, A.D. Jamthikar, L. Saba, D. Gupta, A. Sharma, B. Loi, J.R. Laird, N.N. Khanna, J.S. Suri, A survey on coronary atherosclerotic plaque tissue characterization in intravascular optical coherence tomography, Curr. Atheroscler. Rep. 20 (2018) 33, https://doi.org/10.1007/s11883-018-0736-8.

[11] L. Di Vito, M. Agozzino, V. Marco, A. Ricciardi, M. Concardi, E. Romagnoli, L. Gatto, G. Calogero, L. Tavazzi, E. Arbustini, F. Prati, Identification and quantification of macrophage presence in coronary atherosclerotic plaques by optical coherence tomography, Eur. Hear. J. - Cardiovasc. Imaging 16 (2015) 807, https://doi.org/10.1093/ehjci/jeu307.

[12] U. Garbin, E. Baggio, C. Stranieri, A. Pasini, S. Manfro, C. Mozzini, P. Vallerio, G. Lipari, F. Merigo, G. Guidi, L. Cominacini, A. Fratta Pasini, Expansion of necrotic core and shedding of Mertk receptor in human carotid plaques: a role for oxidized polyunsaturated fatty acids? Cardiovasc. Res. 97 (2013) 125–133, https://doi.org/10.1093/cvr/cvs301.

[13] H. Tao, P.G. Yancey, V.R. Babaev, J.L. Blakemore, Y. Zhang, L. Ding, S. Fazio, M.F. Linton, Macrophage SR-BI mediates efferocytosis via Src/PI3K/Rac1 signaling and reduces atherosclerotic lesion necrosis, J. Lipid Res. 56 (2015) 1449–1460, https://doi.org/10.1194/jlr.M056689.

[14] E. Thorp, G. Li, T.A. Seimon, G. Kuriakose, D. Ron, I. Tabas, Reduced apoptosis and plaque necrosis in advanced atherosclerotic lesions of apoe-/- and ldlr-/- mice lacking CHOP, Cell Metabol. 9 (2009) 474–481, https://doi.org/10.1016/j.cmet.2009.03.003.

[15] T.A. Seimon, M.J. Nadolski, X. Liao, J. Magallon, M. Nguyen, N.T. Feric, M.L. Koschinsky, R. Harkewicz, J.L. Witztum, S. Tsimikas, D. Golenbock, K.J. Moore, I. Tabas, Atherogenic lipids and lipoproteins trigger CD36-TLR2-dependent apoptosis in macrophages undergoing endoplasmic reticulum stress, Cell Metabol. 12 (2010) 467–482, https://doi.org/10.1016/j.cmet.2010.09.010.

[16] P. Libby, Collagenases and cracks in the plaque, J. Clin. Investig. 123 (2013) 3201–3203, https://doi.org/10.1172/JCI67526.

[17] I. Tabas, K.E. Bornfeldt, Macrophage phenotype and function in different stages of atherosclerosis, Circ. Res. 118 (2016) 653–667, https://doi.org/10.1161/CIRCRESAHA.115.306256.

[18] M. Drechsler, R. de Jong, J. Rossaint, J.R. Viola, G. Leoni, J.M. Wang, J. Grommes, R. Hinkel, C. Kupatt, C. Weber, Y. Doring, A. Zarbock, O. Soehnlein, Annexin A1 counteracts chemokine-induced arterial myeloid cell recruitment, Circ. Res. 116 (2015) 827–835, https://doi.org/10.1161/CIRCRESAHA.116.305825.

[19] D.R. Lewis, L.K. Petersen, A.W. York, K.R. Zablocki, L.B. Joseph, V. Kholodovych, R.K. Prud'homme, K.E. Uhrich, P.V. Moghe, Sugar-based amphiphilic nanoparticles arrest atherosclerosis in vivo, Proc. Natl. Acad. Sci. 112 (2015) 2693–2698, https://doi.org/10.1073/pnas.1424594112.

[20] R. Duivenvoorden, J. Tang, D.P. Cormode, A.J. Mieszawska, D. Izquierdo-Garcia, C. Ozcan, M.J. Otten, N. Zaidi, M.E. Lobatto, S.M. van Rijs, B. Priem, E.L. Kuan, C. Martel, B. Hewing, H. Sager, M. Nahrendorf, G.J. Randolph, E.S.G. Stroes, V. Fuster, E.A. Fisher, Z.A. Fayad, W.J.M. Mulder, A statin-loaded reconstituted high-density lipoprotein nanoparticle inhibits atherosclerotic plaque inflammation, Nat. Commun. 5 (2014) 3065, https://doi.org/10.1038/ncomms4065.

[21] J.M. Tarkin, M.R. Dweck, N.R. Evans, R.A.P. Takx, A.J. Brown, A. Tawakol, Z.A. Fayad, J.H.F. Rudd, Imaging atherosclerosis, circ, Res 118 (2016) 750–769, https://doi.org/10.1161/CIRCRESAHA.115.306247.

[22] E. Thorp, G. Li, T.A. Seimon, G. Kuriakose, D. Ron, I. Tabas, Reduced apoptosis and plaque necrosis in advanced atherosclerotic lesions of Apoe−/− and Ldlr−/− mice lacking CHOP, Cell Metabol. 9 (2009) 474–481, https://doi.org/10.1016/j.cmet.2009.03.003.

[23] E. Romagnoli, L. Gatto, F. Prati, The CLIMA study: assessing the risk of myocardial infarction with a new anatomical score, Eur. Heart J. Suppl. 21 (2019) B80–B83, https://doi.org/10.1093/eurheartj/suz032.
[24] G. Zahnd, A. Hoogendoorn, Nicolas Combaret, A. Karanasos, E. Péry, Laurent Sarry, Pascal Motreff, W. Niessen, E. Regar, Gijs Van Soest, Frank Gijsen, T. Van Walsum, Contour segmentation of the intima, media, and adventitia layers in intracoronary OCT images: application to fully automatic detection of healthy wall regions, Int J CARS (2017), https://doi.org/10.1007/s11548-017-1657-7 (n.d.).
[25] G.-A. Cheimariotis, Y.S. Chatzizisis, V.G. Koutkias, K. Toutouzas, A. Giannopoulos, M. Riga, I. Chouvarda, A.P. Antoniadis, C. Doulaverakis, I. Tsamboulatidis, I. Kompatsiaris, G.D. Giannoglou, N. Maglaveras, Arc-oct: automatic detection of lumen border in intravascular OCT images, Comput. Methods Progr. Biomed. 151 (2017) 21–32, https://doi.org/10.1016/j.cmpb.2017.08.007.